nature electronics

ARTICLES

https://doi.org/10.1038/s41928-022-00722-0

Check for updates

A hole spin qubit in a fin field-effect transistor above 4 kelvin

Leon C. Camenzind[1,3], Simon Geyer[1,3], Andreas Fuhrer[2], Richard J. Warburton[1], Dominik M. Zumbühl[1]✉ and Andreas V. Kuhlmann[1,2]✉

The greatest challenge in quantum computing is achieving scalability. Classical computing, which previously faced such issues, currently relies on silicon chips hosting billions of fin field-effect transistors. These devices are small enough for quantum applications: at low temperatures, an electron or hole trapped under the gate can serve as a spin qubit. Such an approach potentially allows the quantum hardware and its classical control electronics to be integrated on the same chip. However, this requires qubit operation at temperatures above 1 K, where the cooling overcomes heat dissipation. Here we show that silicon fin field-effect transistors can host spin qubits operating above 4 K. We achieve fast electrical control of hole spins with driving frequencies up to 150 MHz, single-qubit gate fidelities at the fault-tolerance threshold and a Rabi-oscillation quality factor greater than 87. Our devices feature both industry compatibility and quality, and are fabricated in a flexible and agile way that should accelerate further development.

Quantum dot (QD) spin qubits[1] in silicon have potential applications in large-scale quantum computation[2] due to their long coherence times[3] and high quality factors[4–6], as well as the fact that complementary metal–oxide–semiconductor (CMOS) manufacturing processes[7–9] can be used to create dense arrays of interconnected spin qubits[10,11]. Inspired by conventional integrated circuits, the on-chip integration of classical control electronics with the qubit array has been suggested as a way to overcome the challenges in wiring up large numbers of multiterminal QD devices[12]. However, since the electronics produce heat, the amount of control functionality that can be implemented depends on the available cooling power. Therefore, it is beneficial to be able to operate qubits at temperatures greater than 1 K, where cooling power is orders of magnitude higher than at millikelvin temperatures[13,14]. For example, Intel's cryogenic control chip, which is known as Horse Ridge, works at 3 K (ref. [15]).

Spin qubits come in two distinct forms: electron[3–5,13,14,16] and hole[7,17–20]. With electrons, an artificial spin–orbit interaction (SOI) can be engineered by equipping the qubit with a micromagnet[4,5,16]. Conversely, hole spins experience a strong intrinsic SOI[21]. All-electrical spin control is achieved via electric-dipole spin resonance (EDSR)[22–26], where an applied oscillating electric field induces spin rotations. Compared with electrons, holes can reduce device complexity, which benefits scalability, because no additional device components are required to generate the SOI. Furthermore, with holes in silicon nanowires or fin field-effect transistors (FinFETs)[27–29], the SOI can be exceptionally strong and fully tunable, creating a switchable coupling strength and a way to mitigate the effects of charge noise[20,21,30]. Moreover, hole spins are better protected against nuclear spin noise due to their weak hyperfine interaction[31].

Recently, electron spin qubits operating at up to 1.5 K have been demonstrated[13,14]. In this Article, we report hole spin qubits working at 1.5–5.0 K, that is, in a temperature range where thermal energy is much larger than the qubit level splitting and cryogenic control electronics can be operated[15]. Hole spin qubits are integrated in silicon FinFET devices that are created using standard CMOS fabrication techniques, including self-aligned gates and chemically selective plasma etches instead of lift-off processes[8,9]. In addition, a high degree of process flexibility and short turnaround are achieved by using electron-beam lithography instead of advanced optical lithography[32]. The fin provides an one-dimensional confinement for holes, enabling fast and electrically tunable effective spin-1/2 qubits[20,21,30]. We demonstrate EDSR-based spin control with Rabi frequencies up to 150 MHz and voltage-tunable qubit frequencies, a feature employed to implement z rotations as fast as 45 MHz. We also show spin rotations around the x and y axes of the Bloch sphere with a single-qubit gate fidelity of 98.9% at 1.5 K. A high robustness against temperature allows for qubit operation above the boiling point of liquid ^{4}He, although with a reduced dephasing time T_2^* compared with 1.5 K, which is consistent with an observed whitening of the spectral noise density on increasing temperature.

Electrical control of hole spins

A tilted side view from a scanning electron microscope and a cross-sectional view from a transmission electron microscope of a co-fabricated device are shown in Fig. 1a,b. Since these FinFETs are fabricated using CMOS processes, they feature a highly uniform gate profile[32] and ultrasmall gate lengths[9], resulting in an estimated effective dot size of ~7 nm (Supplementary Section 6). By negatively biasing the gate electrodes, an accumulation-mode hole double quantum dot (DQD), hosting two individual spin-1/2 qubits, is formed[9]. Here a pseudospin of $\pm 1/2$ is assigned to the two lowest-energy hole states, which for one-dimensional-like hole systems can have large contributions of both heavy-hole and light-hole basis states[21,30]. We measure the direct current $I_{\mathrm{d.c.}}$ through the DQD, which when combined with spin-to-charge conversion through Pauli spin blockade (PSB)[33,34] provides qubit readout functionality (Methods provides further details on the device and measurement setup). For the device investigated, PSB is observed for the $(1,1) \rightarrow (0,2)/(2,0)$ charge-state transitions, and no additional transitions are observed when further depleting the QDs. Here (m,n)

[1]Department of Physics, University of Basel, Basel, Switzerland. [2]IBM Research—Zürich, Rüschlikon, Switzerland. [3]These authors contributed equally: Leon C. Camenzind, Simon Geyer. ✉e-mail: dominik.zumbuhl@unibas.ch; andreas.kuhlmann@unibas.ch

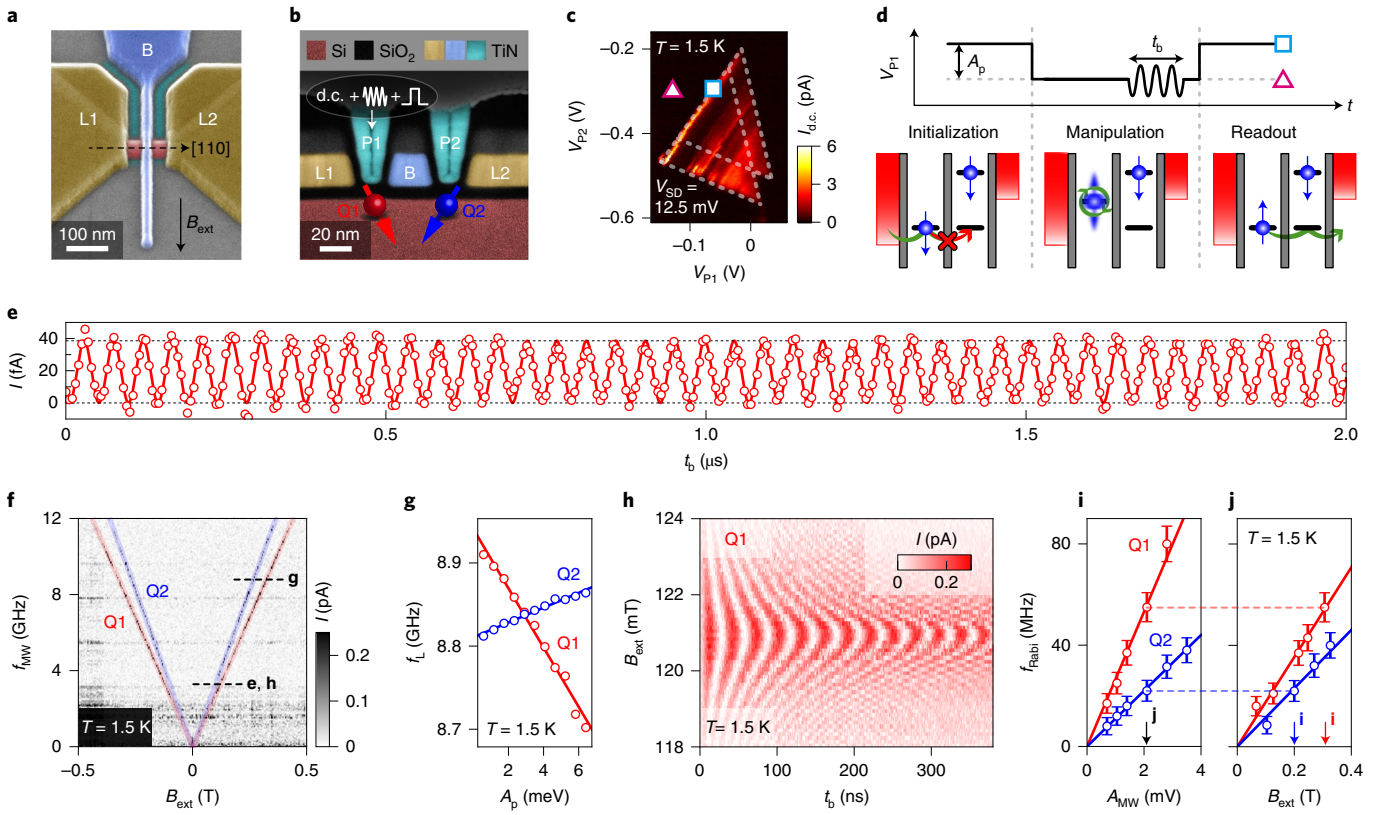

Fig. 1 | Spin-orbit qubits in a FinFET. a, False-colour scanning electron microscopy image of an unfinished device showing the two lead gates L1 and L2 (yellow) as well as the interdot barrier gate B (blue; ~35 nm). An in-plane external magnetic field B_{ext} is applied perpendicular to the fin (red). **b**, Cross-sectional transmission electron microscopy image along the black dashed line in **a** after the integration of the QDs' plunger gates P1 and P2 (turquoise; ~15 nm). In addition to a d.c. voltage, fast pulses and microwaves can be applied to P1. The current flow is observed from source to drain via the fin-shaped channel. **c**, Measurement of a spin-blocked pair of bias triangles. The blue square and pink triangle mark the qubit initialization/readout and manipulation point, respectively. **d**, Schematic of the spin manipulation cycle with the corresponding pulse scheme. **e**, Rabi oscillation with f_{Rabi} = 22 MHz measured on Q1 at B_{ext} = 123 mT, f_{MW} = 3.311 GHz, A_{MW} = 1.1 mV and T = 1.5 K. The data have been corrected by removing a small constant offset, and are fitted (solid curve) to $I(t_b) = A\sin(2\pi f_{Rabi} t_b + \theta) + B$, where A, B, f_{Rabi} and θ are the fit parameters. **f**, Measurement of current as a function of f_{MW} and B_{ext}. Along the red (blue) line, the spin resonance condition is met for Q1 (Q2). For each frequency, the average current has been subtracted. **g**, Electrical tunability of the qubit frequency with the depth of the Coulomb pulse. The solid lines represent linear fits to the data. **h**, Detuned Rabi oscillations showing a typical chevron pattern, measured at f_{MW} = 3.311 GHz and A_{MW} = 1.4 mV. **i**,**j**, Dependence of f_{Rabi} on A_{MW} (**i**) and B_{ext} (**j**). The solid lines are linear fits to the data with zero offset. Error bars correspond to 1σ.

denotes the effective hole occupancy of the left/right QD, whereas the true hole occupancy is $(m+m_0, n+n_0)$ with possible additional holes m_0 and n_0.

In the PSB regime, hole tunnelling is forbidden by spin conservation if the two spins—one per QD—occupy a spin-polarized triplet state ($|(1,1)T_+\rangle$ or $|(1,1)T_-\rangle$) and are thus aligned parallel. The unpolarized triplet $|(1,1)T_0\rangle$ is not blockaded as it mixes with the singlet $|(1,1)S\rangle$, which itself is coupled to the singlet $|(0,2)S\rangle$ such that hole transport occurs[35]. Spin blockade can be lifted by flipping the direction of one hole spin using EDSR[7,17,20,23,24], which is performed by applying square voltage pulses and microwave (MW) bursts to gate P1 (Fig. 1b). The measurements consist of three stages (Fig. 1c,d): first, the two hole spins are initialized in a polarized spin state through PSB. Then, the system is pulsed into Coulomb blockade, where the MW signal is applied. Finally, in the readout stage, a current is detected if the spins are antiparallel, such that one hole can tunnel into the neighbouring QD and exit into the nearby reservoir. This cycle is repeated many times for a measurable current, such that the duration of the manipulation stage is limited to a few microseconds (Supplementary Section 1).

For the high-temperature operation of spin qubits[13,14], spin-to-charge conversion via PSB rather than energy-selective tunnelling[36] is favourable, since the single-dot singlet–triplet splitting[9] is typically much larger than the Zeeman energy. Thus, the measurements can be performed at higher temperature and smaller external magnetic field, resulting in lower and technically less demanding qubit frequencies.

EDSR takes place under the condition that the MW frequency f_{MW} equals the Larmor frequency $f_L = |g^*|\mu_B|B_{ext}|/h$, where g^* denotes the effective hole Landé g factor along the magnetic-field (B_{ext}) direction, μ_B Bohr's magneton and h Planck's constant. In Fig. 1f, the resonance appears as a V shape that maps out f_L in the f_{MW}–B_{ext} plane. The single-hole spin resonance conditions differ slightly for the two qubits (Q1 and Q2), making them individually addressable. From the slope of the current lines, we extract the absolute values for the g^* factor as 1.94 ± 0.05 and 2.35 ± 0.05. These two different values indicate a sensitivity to the local electric fields, which also provides an additional control knob for the g^* factor and thus the qubit frequency[3,5,18,20,26]. This is confirmed by Fig. 1g, where the f_L dependence on the square pulse amplitude A_p is shown.

When the MW drive is on resonance, the DQD current reveals Rabi oscillations as a function of burst duration t_b. An example of a 22 MHz Rabi oscillation, whose decay time is too long to be observed within 87π rotations, corresponding to the longest

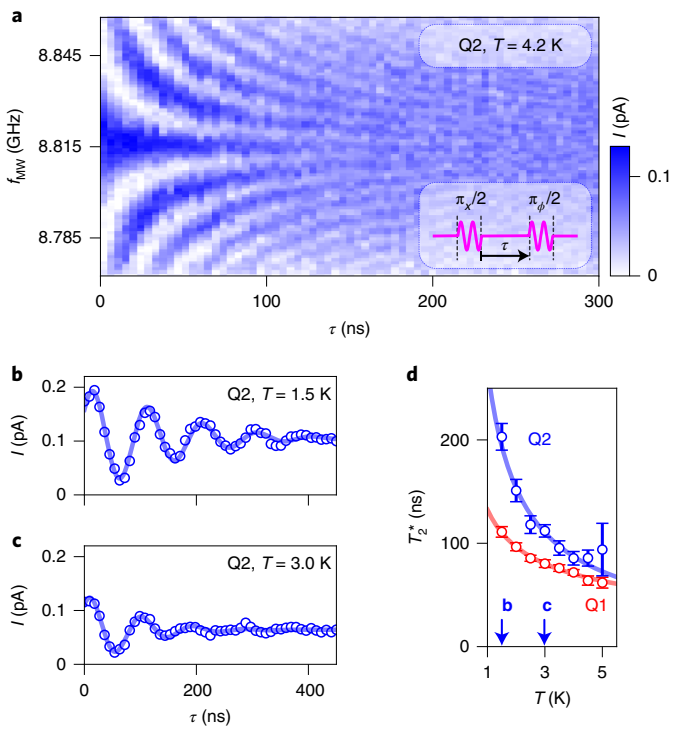

Fig. 2 | Hot qubit coherence. a, Ramsey fringe experiment performed at 4.2 K. B_{ext} is fixed at 267 mT. The pulse sequence, which consists of two 15-ns-long $\frac{\pi}{2}$ bursts separated by waiting time τ, is illustrated in the bottom-right inset. ϕ denotes the phase of the second pulse with respect to the first one; here $\phi = 0$. **b**,**c**, Decay of Ramsey fringes at 1.5 K (**b**) and 3.0 K (**c**). The data were taken on resonance with a τ-dependent phase $\phi(\tau)$, which adds an artificial oscillation[50]. The solid curves show fits to $A + B\sin(\omega\tau + \theta)\exp[-(\tau/T_2^*)^{\beta+1}]$ with temperature-dependent β. **d**, Temperature dependence of the spin-dephasing time, revealing a power-law decay $T_2^* \propto T^{-\eta}$, where $\eta = 0.46 \pm 0.02$ for Q1 and $\eta = 0.81 \pm 0.06$ for Q2. Error bars correspond to 1σ.

applicable t_b, is given in Fig. 1d. For a detuned f_{MW}, the qubit rotates around a tilted axis on the Bloch sphere, resulting in faster rotations of reduced contrast, as demonstrated by the chevron pattern in Fig. 1h. The Rabi frequency f_{Rabi} linearly increases not only with the MW amplitude A_{MW} (Fig. 1i) but also B_{ext} (Fig. 1j), as expected for SOI-mediated spin rotations[20,22,23,25,26]. For these measurements, A_{MW} is calibrated using the photon-assisted tunnelling response (Supplementary Section 3)[23]. The maximum f_{Rabi} observed is 147 MHz (Supplementary Section 5), which corresponds to a spin-flip time of just ~3.4 ns. Under the assumption that EDSR occurs due to a periodic displacement of the wavefunction as a whole, the g^* factor is not modulated[26] and f_{Rabi} depends on the spin–orbit length l_{SO} (ref. [23]). We can, therefore, state an estimate for l_{SO} in the range of 20 to 60 nm (Supplementary Section 7), that is, similar values to the one reported before[9] and in very good agreement with theory predictions[21].

A key parameter for qubit controllability is the quality factor defined as $Q = 2f_{Rabi}T_2^{Rabi}$, where T_2^{Rabi} is the decay time of the Rabi oscillations. For the data presented in Fig. 1e, no decay is observed within ~2 µs, that is, $Q \gg 87$. In terms of quality factors, our hole spin qubits, therefore, outperform their hot electron counterparts[13,14].

Hole spin coherence

Next, we evaluate the spin coherence by performing a Ramsey experiment. Here two $\frac{\pi}{2}$ pulses separated by delay time τ (during which the qubit can freely evolve and dephase) are applied. When f_{MW} is detuned from the qubit resonance, the current through the device shows coherent oscillations known as Ramsey fringes. The data in Fig. 2a are measured at a temperature of $T = 4.2$ K, which corresponds to the boiling point of liquid ^{4}He and can be achieved in a technically non-demanding way by immersing the sample in a liquid ^{4}He bath or at the second stage of a dry pulse-tube refrigerator. The dephasing time T_2^* is determined by fitting the envelope of the fringe decay to $\exp(-(\tau/T_2^*)^{\beta(T)+1})$, where β depends on the temperature (discussed later). Despite the fact that our qubit readout is protected against temperature by the large orbital energies, which exceed the thermal energy available at 4.2 K by an order of magnitude, a degradation of the signal contrast on increasing temperature is observed (Fig. 2b,c). The reasons for this are not yet fully understood; however, we speculate that this is due to spin-flip co-tunnelling (Supplementary Section 8). The T dependence of T_2^* in the range of 1.5–5.0 K is presented for both qubits (Fig. 2d). Although Q1 can be manipulated faster than Q2, it lags behind in coherence. The spin-dephasing time drops with increasing temperature, described by a power-law decay ($\propto T^{-\eta}$), where $\eta = 0.5$ (0.8) for Q1 (Q2)—a rather weak temperature dependence similar to previous reports[13,14]. The obtained values for T_2^* are consistent with the EDSR spectral width (Supplementary Section 9), and a spin relaxation time $T_1 > 10$ µs was found at 4.2 K (Supplementary Section 12). In the following, the focus is on the more coherent Q2.

Single-qubit gate fidelity

Spin rotations around at least two different axes are required to reach any point on the Bloch sphere. In Fig. 3a, we demonstrate two-axis qubit control at both 1.5 and 4.2 K by employing a Hahn-type echo sequence. A modulation of the relative phase ϕ of the second $\frac{\pi}{2}$ pulse yields a set of Ramsey fringes that are phase shifted by π for a π_x and π_y echo pulse, which is applied to extend the coherence. The performance of the hole spin rotations is characterized using randomized benchmarking[37,38] (Fig. 3b and Methods). At 1.5 K, a single-qubit gate fidelity of $F_s = 98.9 \pm 0.2\%$ is obtained, which is at the fault-tolerance level[2,3] and very similar to the values recently reported for hot electron spin qubits[13,14]. The fidelity is reduced to $F_s = 98.6 \pm 1.6\%$ ($97.9 \pm 1.1\%$) at 3.0 K (4.2 K), revealing a similar scaling with temperature as T_2^*. We, thus, expect to be able to enhance the gate fidelities further by improving the qubit coherence, as well as by optimization of the gate pulses[39].

Besides rotations around the x and y axis of the Bloch sphere, z rotations can be realized by exploiting the electrical tunability of the qubit frequency (Fig. 1g). For this purpose, a square pulse of amplitude A_Z and duration t_Z is added to a Hahn echo sequence (Fig. 3c) to rapidly detune the spin precession frequency, which leads to a phase pick up around the z axis of the Bloch sphere[5]. As a consequence, the DQD current oscillates as a function of t_Z (Fig. 3d) at a frequency that linearly increases with A_Z up to ~45 MHz (Fig. 3e).

Noise spectroscopy

Finally, to gain an insight into the sources of decoherence, we perform noise spectroscopy by employing Carr–Purcell–Meiboom–Gill (CPMG) pulse sequences[40], where a series of n_π π_y pulses are applied as a spectral filter for the environmental noise[5,41,42]. For a power-law noise spectrum $S(f) \propto f^{-\beta}$, the CPMG coherence time T_2^{CPMG} is expected to scale as $T_2^{CPMG} \propto (n_\pi)^{\frac{\beta}{1+\beta}}$ (ref. [42]). This dependency is confirmed in Fig. 4a, and a β value of 0.88 ± 0.11 (0.26 ± 0.03) is determined for 1.5 K (3.0 K), revealing a whitening of the noise on increasing the temperature and thus a reduced noise-decoupling efficiency. For $n_\pi = 32$, the maximum n_π achievable with our transport-based readout scheme, the hole spin coherence time is extended to 5.4 µs at 1.5 K, which corresponds to an increase by a factor of 27 compared with the unprotected qubit. Although our CPMG measurements are sensitive to noise at frequencies of $f \approx 10^5$–10^7 Hz, we independently probe $S(f)$ at $f \approx 10^{-3}$–10^{-1} Hz by

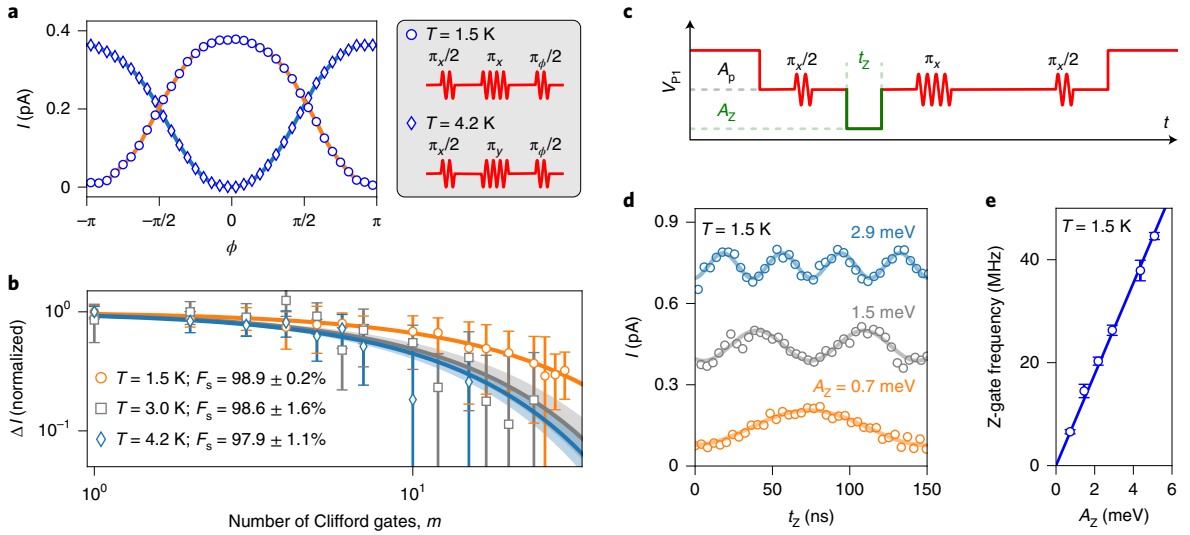

Fig. 3 | X, Y and Z qubit gates. a, Demonstration of two-axis qubit control by applying a Hahn-type echo sequence, where the relative phase ϕ of the second $\frac{\pi}{2}$ pulse is varied. The measurements at 1.5 K (circles) and 4.2 K (diamonds) are phase shifted by π due to the two orthogonal echo pulses (right). **b**, Standard randomized benchmarking at 1.5 K (circles), 3.0 K (squares) and 4.2 K (diamonds) is performed by applying a varying number of Clifford gates m and preparing either a $|\uparrow\rangle$ or $|\downarrow\rangle$ final state. The normalized difference of currents is fitted to a single exponential decay to extract the single-qubit gate fidelities F_s (Methods). The shaded regions show the 1σ error range of the fit parameters. The maximum m decreases with increasing temperature due to a reduced readout contrast. **c**, Schematic of the pulse scheme used to demonstrate qubit rotations around the z axis of the Bloch sphere. In a modified Hahn echo sequence, a square pulse of amplitude A_Z and duration t_Z is applied to shift the qubit precession frequency (Fig. 1g). The resulting phase-shift-induced oscillations are shown in **d** for different A_Z values. The solid curves represent fits to a sinusoidal function, where the oscillation frequency is given by the induced qubit frequency shift. The traces are offset by an increment of 0.3 for clarity. **e**, Speed of z rotations linearly increases with A_Z. The solid line represents a linear fit to the data, yielding a frequency shift of 8.9 MHz meV^{-1}. The data presented in this figure are taken for Q2 at $f_{MW} = 8.812$ GHz. Error bars correspond to 1σ.

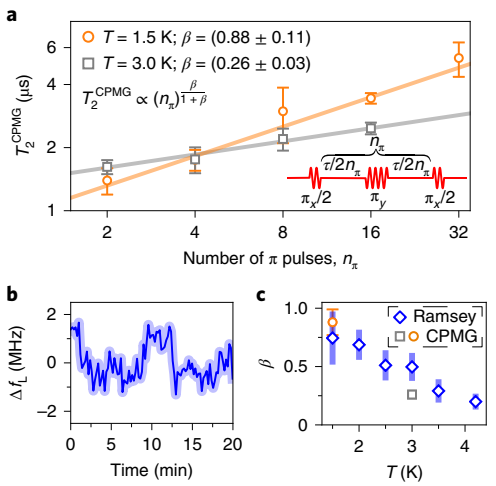

Fig. 4 | Dynamical decoupling and noise spectroscopy. a, Spin coherence time can be enhanced by decoupling the qubit from low-frequency noise using a CPMG pulse sequence (bottom right). A power-law dependence of the coherence time on the number of refocusing pulses n_π is confirmed by fitting (solid lines) the data to $T_2^{CPMG} = T_2^0 (n_\pi)^{\frac{\beta}{1+\beta}}$, where β represents the scaling exponent of a power-law noise spectrum, namely, $S(f) \propto f^{-\beta}$. **b**, Time trace of the qubit frequency obtained from repeated Ramsey measurements. The shaded region indicates the frequency uncertainty due to readout noise. **c**, Temperature dependence of the noise exponent β extracted from either CPMG or Ramsey measurements. The data presented in this figure are taken for Q2 at $f_{MW} = 8.812$ GHz. Error bars correspond to 1σ.

tracking Larmor-frequency fluctuations through repeated Ramsey experiments[5] (Fig. 4b). The temperature dependence of β demonstrates noise whitening in both frequency ranges, and the good agreement of the β values for the two frequency windows suggests a similar coloured noise spectrum over a wide range of frequencies. From the scaling of β with T, we cannot uniquely identify the underlying noise sources, such as charge or nuclear spin fluctuations[43]. We note, however, that the longest T_2^* measured is ~440 ns (Supplementary Section 10), which does not only exceed the dephasing times reported so far for hole spins in silicon at millikelvin temperatures[44] but is also close to the estimated limit of ~500 ns set by the hole–spin hyperfine interaction (Supplementary Section 11). This sub-microsecond limit is a consequence of the hole spins interacting with a relatively small number of nuclear spins $N_s \approx 310$, which increases the Overhauser field fluctuations that scale with $1/\sqrt{N_s}$ (ref. [45]) and also represents a lower bound due to the anisotropy of the hole hyperfine interaction[31].

Conclusions

We have reported hole spin qubits in silicon FinFETs that operate above 4 K. The strong SOI allows for spin rotations as fast as 147 MHz and the weak hyperfine coupling ensures T_2^* of up to 440 ns. In addition to two-axis control, we implement fast z rotations by employing the electrical tunability of the $g^\star$ factor. At 1.5 K, we achieve fault-tolerant single-qubit gate fidelities. These results have been achieved using an industry-compatible FinFET device architecture, which is also well suited to the implementation of larger arrays of interacting qubits, such as a linear chain of exchange-coupled QD spins. Connectivity beyond the nearest neighbours can be realized by coupling to a superconducting MW resonator[46] or coherent spin shuttling[47].

In the quest for a higher qubit quality factor, hyperfine-induced dephasing can be prevented by engineering a nearly nuclear-spin-free environment[3]. Although a stronger SOI results in shorter gate times, it also increases the susceptibility to charge noise. For hole spins in silicon FinFETs, however, an unusually strong and at the same time electrically tunable SOI, allowing for on-demand switching

between qubit idling and manipulation modes, has been predicted[20,21,30]. Furthermore, a fast single-shot readout of hole spins is required for accurate qubit measurements. At few-kelvin temperatures, this can be realized using a DQD charge sensor that exploits tunnelling between two quantized states[48]. This technique is more resilient against temperature than a single-sensor QD, and high-fidelity single-shot readout up to 8 K at a bandwidth greater than 100 kHz was demonstrated. In addition, a read-time resolution of <1 µs, which is fast compared with our hole spin lifetime, was demonstrated using radio-frequency reflectometry of a silicon DQD[49]. These readout techniques can be combined with the advance reported here—a hole spin qubit in a FinFET at temperatures of 4 K and above.

Methods

Device fabrication. The fin structures are defined along the [110] direction on a near-intrinsic, natural silicon substrate ($\rho > 10\,k\Omega\,cm$ and (100) surface) by means of electron-beam lithography (EBL) and dry etching[9]. The gate oxide is formed by thermal oxidation of silicon, yielding a ≃7-nm-thick silicon dioxide (SiO_2) layer, which is covered by ≃20 nm titanium nitride (TiN) grown by atomic layer deposition. The first layer of gates containing L1, L2 and B is patterned using EBL and dry etching. Subsequently, the gate stack (≃4.5 nm SiO_x and ≃20.0 nm TiN) of the second gate layer hosting P1 and P2 is grown by atomic layer deposition. The plunger gates are implemented by means of a self-aligned process[9], where the gaps between the gates of the first gate layer (Fig. 1a, turquoise) act as a template for the plunger gates. The gate lengths of the device measured are $l_B \approx 35$ nm and $l_P \approx 15$ nm. The source and drain contacts are p- type and made of platinum silicide (PtSi), which is formed by sputtering a ≃15-nm-thick Pt layer on a silicon surface cleaned beforehand, followed by silicidation annealing at 450 °C for 10 min in an argon atmosphere. Finally, the devices are encapsulated in a ≃100-nm-thick SiO_2 layer that is grown by plasma-enhanced chemical vapour deposition and are accessed via tungsten interconnects.

Experimental setup. All the measurements are performed using a variable-temperature insert that can be operated at 1.5–50.0 K. The MW and d.c. signals can be simultaneously applied to gate P1 (Fig. 1b) via a bias tee on the sample board. The d.c. voltages are supplied by a low-noise voltage source (BasPI SP927) and the source–drain current is measured with a current-to-voltage amplifier at a gain of 10^9 (BasPI SP983c). A square voltage pulse used to drive the device between Coulomb blockade (qubit manipulation stage) and PSB (qubit initialization and readout stage) is provided by an arbitrary waveform generator (Tektronix AWG5204), which also controls the *I* and *Q* inputs of a vector signal generator (Keysight E8267D) to generate phase-controlled square-shaped MW bursts. The latter ones and the square pulse are combined using a wideband power combiner (Mini-Circuits ZC2PD-5R263-S+). The qubit readout current is distinguished from the background by chopping the MW signal at a frequency of 89.2 Hz and demodulating the current at this frequency with a lock-in amplifier (Signal Recovery 7265). Supplementary Section 1 provides further details.

Clifford benchmarking protocol. Randomized benchmarking is performed by applying a randomized sequence of a varying number of Clifford gates *m* before the spin state is rotated such that the final state ideally becomes either the $|\uparrow\rangle$ or $|\downarrow\rangle$ state. Each of the 24 gates in the Clifford group is constructed from the set $\{I, \pm X, \pm Y, \pm X/2, \pm Y/2\}$, with I being the identity gate[38]. Assuming that the qubit initial state is $|\downarrow\rangle$, a current flow is only observed when the spin blockade is lifted for a final $|\uparrow\rangle$ state. Thus, the difference in current between the sequences designed to output either a $|\uparrow\rangle$ or $|\downarrow\rangle$ state, that is, $\Delta I = I^{|\uparrow\rangle} - I^{|\downarrow\rangle}$, is proportional to the probability $p_\uparrow^{|\uparrow\rangle} - p_\uparrow^{|\downarrow\rangle}$. For each *m*, we average over 10 randomized sequences and the average Clifford-gate fidelity F_C is obtained from fitting the normalized current difference to $(2F_C - 1)^m$. Since a Clifford gate consists of 1.875 gates on average, the average single-qubit gate fidelity F_s is derived from $F_s = 1 - (1 - F_C)/1.875$.

Data availability

The data supporting the plots within this paper are available at the Zenodo repository: https://doi.org/10.5281/zenodo.4579586

Received: 30 March 2021; Accepted: 21 January 2022;
Published online: 03 March 2022

References

1. Loss, D. & DiVincenzo, D. P. Quantum computation with quantum dots. *Phys. Rev. A* **57**, 120 (1998).
2. Fowler, A. G., Mariantoni, M., Martinis, J. M. & Cleland, A. N. Surface codes: towards practical large-scale quantum computation. *Phys. Rev. A* **86**, 032324 (2012).
3. Veldhorst, M. et al. An addressable quantum dot qubit with fault-tolerant control-fidelity. *Nat. Nanotechnol.* **9**, 981–985 (2014).
4. Takeda, K. et al. A fault-tolerant addressable spin qubit in a natural silicon quantum dot. *Sci. Adv.* **2**, e1600694 (2016).
5. Yoneda, J. et al. A quantum-dot spin qubit with coherence limited by charge noise and fidelity higher than 99.9%. *Nat. Nanotechnol.* **13**, 102–106 (2017).
6. Yang, C. H. et al. Silicon qubit fidelities approaching incoherent noise limits via pulse engineering. *Nat. Electron.* **2**, 151–158 (2019).
7. Maurand, R. et al. A CMOS silicon spin qubit. *Nat. Commun.* **7**, 13575 (2016).
8. Kuhlmann, A. V., Deshpande, V., Camenzind, L. C., Zumbühl, D. M. & Fuhrer, A. Ambipolar quantum dots in undoped silicon fin field-effect transistors. *Appl. Phys. Lett.* **113**, 122107 (2018).
9. Geyer, S. et al. Self-aligned gates for scalable silicon quantum computing. *Appl. Phys. Lett.* **118**, 104004 (2021).
10. Vandersypen, L. M. K. et al. Interfacing spin qubits in quantum dots and donors—hot, dense, and coherent. *npj Quantum Inf.* **3**, 34 (2017).
11. Veldhorst, M., Eenink, H. G. J., Yang, C. H. & Dzurak, A. S. Silicon CMOS architecture for a spin-based quantum computer. *Nat. Commun.* **8**, 1766 (2017).
12. Franke, D., Clarke, J., Vandersypen, L. & Veldhorst, M. Rent's rule and extensibility in quantum computing. *Microprocess. Microsyst.* **67**, 1–7 (2019).
13. Petit, L. et al. Universal quantum logic in hot silicon qubits. *Nature* **580**, 355–359 (2020).
14. Yang, C. H. et al. Operation of a silicon quantum processor unit cell above one kelvin. *Nature* **580**, 350–354 (2020).
15. Xue, X. et al. CMOS-based cryogenic control of silicon quantum circuits. *Nature* **593**, 205–210 (2021).
16. Kawakami, E. et al. Electrical control of a long-lived spin qubit in a Si/SiGe quantum dot. *Nat. Nanotechnol.* **9**, 666–670 (2014).
17. Watzinger, H. et al. A germanium hole spin qubit. *Nat. Commun.* **9**, 3902 (2018).
18. Hendrickx, N. W. et al. A single-hole spin qubit. *Nat. Commun.* **11**, 3478 (2020).
19. Hendrickx, N. W. et al. A four-qubit germanium quantum processor. *Nature* **591**, 580–585 (2021).
20. Froning, F. N. M. et al. Ultrafast hole spin qubit with gate-tunable spin–orbit switch functionality. *Nat. Nanotechnol.* **16**, 308–312 (2021).
21. Kloeffel, C., Rančić, M. J. & Loss, D. Direct Rashba spin-orbit interaction in Si and Ge nanowires with different growth directions. *Phys. Rev. B* **97**, 235422 (2018).
22. Golovach, V. N., Borhani, M. & Loss, D. Electric-dipole-induced spin resonance in quantum dots. *Phys. Rev. B* **74**, 165319 (2006).
23. Nowack, K. C., Koppens, F. H. L., Nazarov, Y. V. & Vandersypen, L. M. K. Coherent control of a single electron spin with electric fields. *Science* **318**, 1430–1433 (2007).
24. Nadj-Perge, S., Frolov, S. M., Bakkers, E. P. A. M. & Kouwenhoven, L. P. Spin–orbit qubit in a semiconductor nanowire. *Nature* **468**, 1084–1087 (2010).
25. Voisin, B. et al. Electrical control of *g*-factor in a few-hole silicon nanowire MOSFET. *Nano Lett.* **16**, 88–92 (2015).
26. Crippa, A. et al. Electrical spin driving by *g*-matrix modulation in spin-orbit qubits. *Phys. Rev. Lett.* **120**, 137702 (2018).
27. Auth, C. et al. A 22nm high performance and low-power CMOS technology featuring fully-depleted tri-gate transistors, self-aligned contacts and high density MIM capacitors. In *2012 Symposium on VLSI Technology (VLSIT)* 131–132 (IEEE, 2012).
28. Auth, C. et al. A 10nm high performance and low-power CMOS technology featuring 3rd generation FinFET transistors, self-aligned quad patterning, contact over active gate and cobalt local interconnects. In *2017 IEEE International Electron Devices Meeting (IEDM)* 29.1.1–29.1.4 (IEEE, 2017).
29. Lansbergen, G. P. et al. Gate-induced quantum-confinement transition of a single dopant atom in a silicon FinFET. *Nat. Phys.* **4**, 656–661 (2008).
30. Bosco, S., Hetényi, B. & Loss, D. Hole spin qubits in Si FinFETs with fully tunable spin-orbit coupling and sweet spots for charge noise. *PRX Quantum* **2**, 010348 (2021).
31. Prechtel, J. H. et al. Decoupling a hole spin qubit from the nuclear spins. *Nat. Mater.* **15**, 981–986 (2016).
32. Zwerver, A. M. J. et al. Qubits made by advanced semiconductor manufacturing. Preprint at https://arxiv.org/abs/2101.12650 (2021).
33. Ono, K., Austing, D., Tokura, Y. & Tarucha, S. Current rectification by Pauli exclusion in a weakly coupled double quantum dot system. *Science* **297**, 1313–1317 (2002).
34. Li, R., Hudson, F. E., Dzurak, A. S. & Hamilton, A. R. Pauli spin blockade of heavy holes in a silicon double quantum dot. *Nano Lett.* **15**, 7314–7318 (2015).
35. Seedhouse, A. E. et al. Pauli blockade in silicon quantum dots with spin-orbit control. *PRX Quantum* **2**, 010303 (2021).

36. Elzerman, J. M. et al. Single-shot read-out of an individual electron spin in a quantum dot. *Nature* **430**, 431–435 (2004).
37. Knill, E. et al. Randomized benchmarking of quantum gates. *Phys. Rev. A* **77**, 012307 (2008).
38. Muhonen, J. T. et al. Quantifying the quantum gate fidelity of single-atom spin qubits in silicon by randomized benchmarking. *J. Phys.: Condens. Matter* **27**, 154205 (2015).
39. Kelly, J. et al. Optimal quantum control using randomized benchmarking. *Phys. Rev. Lett.* **112**, 240504 (2014).
40. Meiboom, S. & Gill, D. Modified spin-echo method for measuring nuclear relaxation times. *Rev. Sci. Instrum.* **29**, 688 (1958).
41. Bylander, J. et al. Noise spectroscopy through dynamical decoupling with a superconducting flux qubit. *Nat. Phys.* **7**, 565–570 (2011).
42. Medford, J. et al. Scaling of dynamical decoupling for spin qubits. *Phys. Rev. Lett.* **108**, 086802 (2012).
43. Kuhlmann, A. V. et al. Charge noise and spin noise in a semiconductor quantum device. *Nat. Phys.* **9**, 570–575 (2013).
44. Hutin, L. et al. Si MOS technology for spin-based quantum computing. In *2018 48th European Solid-State Device Research Conference (ESSDERC)* 12–17 (IEEE, 2018).
45. Assali, L. V. C. et al. Hyperfine interactions in silicon quantum dots. *Phys. Rev. B* **83**, 165301 (2011).
46. Borjans, F., Croot, X. G., Mi, X., Gullans, M. J. & Petta, J. R. Resonant microwave-mediated interactions between distant electron spins. *Nature* **577**, 195–198 (2019).
47. Yoneda, J. et al. Coherent spin qubit transport in silicon. *Nat. Commun.* **12**, 4114 (2021).
48. Huang, J. Y. et al. A high-sensitivity charge sensor for silicon qubits above 1 K. *Nano Lett.* **21**, 6328–6335 (2021).
49. Noiri, A. et al. Radio-frequency-detected fast charge sensing in undoped silicon quantum dots. *Nano Lett.* **20**, 947–952 (2020).
50. Watson, T. F. et al. A programmable two-qubit quantum processor in silicon. *Nature* **555**, 633–637 (2018).

Acknowledgements

We thank M. de Kruijf, C. Kloeffel, D. Loss, F. Froning and F. Braakman for fruitful discussions. Moreover, we acknowledge support by the cleanroom operation team, particularly U. Drechsler, A. Olziersky and D. D. Pineda, at the IBM Binnig and Rohrer Nanotechnology Center, as well as technical support at the University of Basel by S. Martin and M. Steinacher. This work was partially supported by the Georg H. Endress Foundation, the NCCR SPIN, the Swiss Nanoscience Institute (SNI), the Swiss NSF (grant no. 179024), and the EU H2020 European Microkelvin Platform EMP (grant no. 824109). L.C.C. acknowledges support by a Swiss NSF mobility fellowship (P2BSP2_200127).

Author contributions

A.V.K., L.C.C., S.G., A.F., R.J.W. and D.M.Z. conceived the project and experiments. A.V.K. and S.G. fabricated the device. L.C.C. and D.M.Z. prepared the cryogenic measurement setup. A.V.K., S.G., L.C.C. and D.M.Z. performed the experiments. A.V.K., L.C.C. and S.G. analysed the data and wrote the manuscript with input from all the authors.

Competing interests

The authors declare no competing interests.

Additional information

Supplementary information The online version contains supplementary material available at https://doi.org/10.1038/s41928-022-00722-0.

Correspondence and requests for materials should be addressed to Dominik M. Zumbühl or Andreas V. Kuhlmann.

Peer review information *Nature Electronics* thanks Xavier Jehl, Andre Saraiva and Tetsufumi Tanamoto for their contribution to the peer review of this work.